

# Characterization of a Very Shallow Water Acoustic Communication Channel

Brian Borowski

Stevens Institute of Technology

Departments of Computer Science and Electrical and Computer Engineering

Castle Point on Hudson

Hoboken, NJ 07030 USA

**Abstract –** Underwater (UW) acoustics are used for communication in a broad range of applications, with increasing numbers near shore in shallow water, including environmental monitoring, disaster prevention, assisted navigation, distributed tactical surveillance, and mine reconnaissance. While considerable efforts have been made to characterize radio frequency (RF) wireless channels, less attention has been given to shallow water acoustic channels. This paper analyzes data gathered in a very shallow estuary and quantifies how the channel's characteristics constrain the design of an acoustic digital communication system. The channel's scattering function, multipath intensity profile, coherence bandwidth, Doppler power spectrum, and coherence time are presented. Amplitude fluctuations over time are displayed, and maximum likelihood estimation is utilized to fit the data to the Rayleigh, Rice, and Nakagami- $m$  distributions often used to model fading channels.

## I. INTRODUCTION

Over the past three decades there has been much research in underwater acoustic communication. While recent years have seen the shift from noncoherent point-to-point communication to developing networks based on coherent reception techniques [1], relatively few papers have focused on the fundamental process of characterizing the underwater acoustic channel. There is no typical underwater channel [2]; each environment possesses different characteristics that will affect the performance of a digital communication system. Measuring and analyzing a channel's parameters is a necessary step for the design of a successful communication system. Moreover, numerous channel measurements are required to build up a database of underwater environments, so that the research community can create a model for more realistically simulating the physical as well as higher layer protocols within a communication system's network stack.

The shallow water acoustic communication channel can be classified as a multipath fading channel. It generally exhibits a long multipath delay spread, which can lead to intersymbol interference (ISI) if the spread exceeds the symbol time of the communication system. The channel typically has significant Doppler spread in the frequency domain, or short coherence time when viewed in the time domain. Communication in estuarine environments is often complicated by ambient noise from both shipping vessels and activity on the surrounding land, such as that in a construction site. The depth of water in

an estuary is extremely shallow; thus, the effects of surface waves and wind speed on an UW acoustic signal are magnified. In addition, estuaries are prone to stratification, the separation of a body of water into layers of similar densities. Fluctuations in the sound speed within a channel cause the refraction of signals, which in turn lead to shadow zones – areas nearly void of acoustic signal.

Some prior efforts to characterize shallow water acoustic channels include the work of Loubet and Jourdain in the 500-meter deep Northern Sea [3], Cook and Zaknich in the 4-meter deep Fremantle Fishing Boat Harbour in Western Australia [4], Dessaalermos in the 30-meter deep New England shelf [5], and Dol et al. in 80-meter and 200-meter deep sections of the Baltic Sea and North Sea [6], respectively. The work presented in this paper focuses on characterizing a 3-meter deep section of the Hudson River estuary. Section II describes the test procedure and experimental conditions. Section III presents the transforms used to process the raw data and create the scattering function, and it provides all the derived measurements – multipath intensity profile, coherence bandwidth, Doppler power spectrum, and coherence time. Section IV discusses the analyses' implications for the design of a digital communication system. Section V summarizes the effort.

## II. EXPERIMENT



Figure 1. Test site for channel sounding experiment

### A. Field Test Details

Stevens Institute of Technology conducted a field test on August 21, 2008, in the Hudson River estuary adjacent to its

campus, as shown in Figure 1. Two boats were used, one for emitting signals – the Phoenix – and the other for recording them – the Savitsky. The Phoenix was also equipped with a hydrophone to record the emitted signals at a distance of 1 meter from the transducer for later reference. The computer system on the Phoenix used the NI USB-6221 [7] data acquisition (DAQ) board; the system on the Savitsky utilized the NI PCI-6123 [8]. All reference and recorded signals were created at 200 ksamples/second. A custom ceramic transducer emitted the signals, while ITC-6050C hydrophones [9] were used for reception.

The channel was about 3 meters deep, and sounding experiments were performed at distances of 505 and 200 meters. The emitter was placed 1 meter below the surface of the water; hydrophones were placed 60 cm from the floor of the estuary. The boats were anchored and motors turned off while data were gathered. Each test consisted of taking CTD measurements prior to channel sounding, recording 30 seconds of ambient noise, playing a comb signal containing 5 sinusoidal components – 35, 45, 60, 75, and 85 kHz – for 1 minute, and repeatedly emitting a 50-ms linear frequency modulated (LFM) chirp signal spanning 20-100 kHz for 30 seconds.

### B. Chirp Signal Restrictions

Analysis of prior measurements in the Hudson River estuary revealed significant noise below 20 kHz and a very short coherence time, which facilitated the choice of sounding signal for this test. The sounding signal must possess good autocorrelation properties as to closely approximate the Dirac delta function. For a LFM chirp signal, the best result is obtained when chirping from 0 Hz up to the Nyquist frequency. However, because of the Hudson's noise in lower frequency bands and lack of low frequency response in the emitter, 20 kHz was chosen as the starting frequency for the chirp signal.

The length of the sounding signal must not exceed the coherence time of the channel, and when played consecutively with no silence in between repetitions, must exceed the channel's multipath spread. With respect to the coherence time restriction, the channel's characteristics need to remain nearly constant over the duration of the sounding signal in order to capture a single undistorted impulse response estimate. As for the multipath spread, since there is no silence in between soundings, all multipath arrivals must appear within the duration of a sounding so that late arrivals do not overlap with the arrivals appearing from subsequent repetitions. When gaps of silence are introduced, this restriction can be eliminated. However, in order to produce the channel's scattering function with enough resolution (wide range of frequencies), the channel needs to be sounded as often as possible per second.

### C. Environmental Conditions

The field test in the Hudson River estuary was conducted on the afternoon of August 21, 2008. Environmental conditions were recorded at the Castle Point Buoy, at 40.74348° latitude and -74.02263° longitude, and downloaded upon the completion

of the experiment from the website for the Urban Ocean Observatory at the Center for Maritime Systems [10]. The 505-meter test was started at 5:14 P.M. At that time, the temperature was 76°F with 55% relative humidity, the wind speed was about 10 knots, and the wind direction was about 159° [11]. Medwin's expression for sound velocity in meters/second [12]

$$c = 1449.2 + 4.6T - 5.5 \times 10^{-2}T^2 + 2.9 \times 10^{-4}T^3 + (1.34 - 10^{-2}T)(S - 35) + 1.6 \times 10^{-2}D, \quad (1)$$

where  $D$  is the depth in meters,  $S$  is the salinity in parts per thousand (ppt), and  $T$  is the temperature in degrees Celsius, was applied to the CTD measurements taken at the start of the test. Other expressions for sound velocity exist; however, the salinity values obtained in the test fall outside the range of acceptable input values for these expressions. Figure 2 shows the temperature, salinity, and derived sound velocity of the water column in the 505-meter test. Since the numeric difference between practical salinity unit (psu) and ppt is small, psu values were used in place of ppt values while generating this graph.

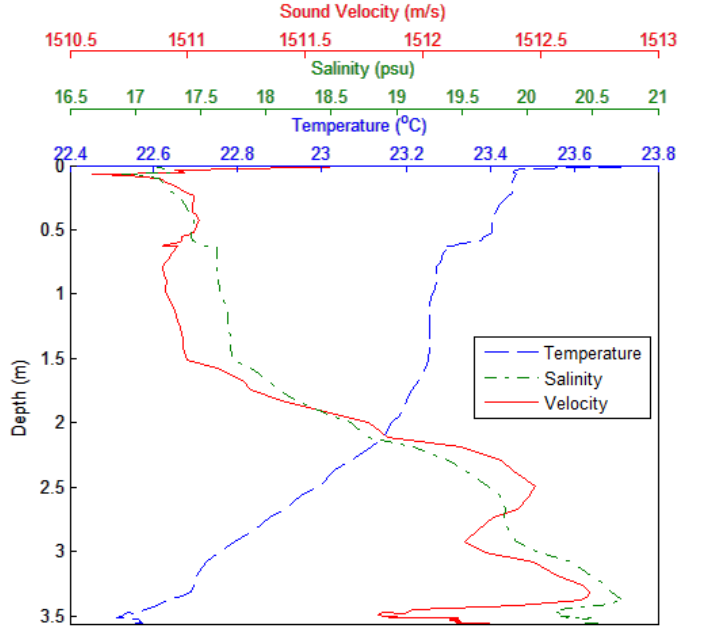


Figure 2. Sound velocity profile for 505-meter channel

The 200-meter test was started at 6:04 P.M. At that time, the temperature was 75°F with 57% relative humidity, the wind speed was about 8 knots, and the wind direction was still about 159°. Following the same procedure as before, the CTD measurements resulted in the sound velocity profile shown in Figure 3.

Ambient noise was recorded for 30 seconds during both tests before any signals were emitted. The power spectral density (PSD) of noise was estimated via a conventional periodogram technique based on a 256-point FFT together with a Hanning window and no overlap. Figure 4 shows the PSD of noise in the Hudson River estuary captured at 5:24 and 6:42 P.M.

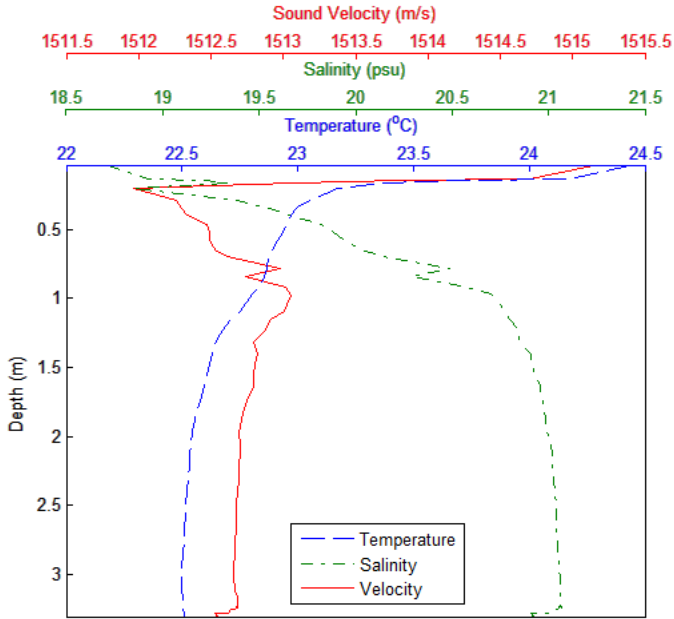


Figure 3. Sound velocity profile for 200-meter channel

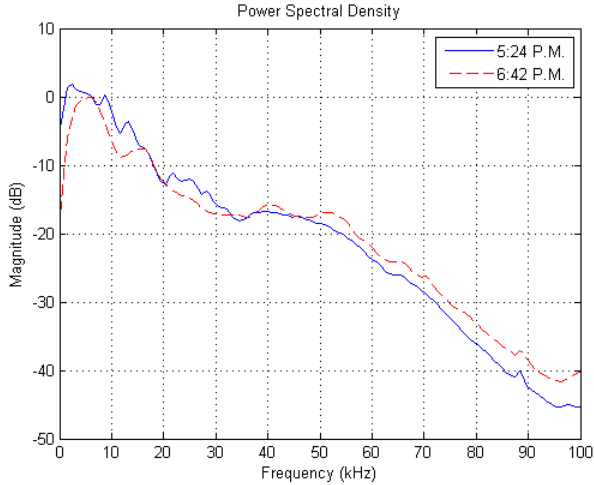


Figure 4. PSD of ambient noise in Hudson River estuary

### III. ANALYSIS

#### A. Time-Variant Impulse Response

Using the wide-sense stationary (WSS) uncorrelated scattering (US) (combined, WSSUS) channel model [13], the time-varying complex-valued low-pass impulse response  $c(\tau; t)$  of the UW channel was captured via the following procedure:

- 1) The 50-ms chirp signals described in Section II were recorded 1 meter from the emitter and either 200 or 505 meters away (depending on the test) where the Savitsky was anchored.
- 2) The received signal and 1-meter reference signal were run through a 10<sup>th</sup> order high-pass Butterworth filter at 20 kHz to eliminate out-of-band noise.
- 3) One chirp was extracted from the 1-meter reference signal, accurate to the sample.
- 4) The imaginary part of the reference chirp signal was

obtained via the Hilbert transform.

- 5) The received signal was cross-correlated with the complex conjugate of the reference chip signal.

There are several experimental issues worth describing in more detail. The standard technique is to apply matched filtering to the received signal with the original waveform sent to the emitter. While this approach results in the best autocorrelation function for a given chirp signal, it unfairly distributes weight to frequencies that were not emitted with equal amplitudes, as in the case when the frequency response of the emitter is not flat. In this situation, the derived impulse response estimates contain higher levels of noise correlation.

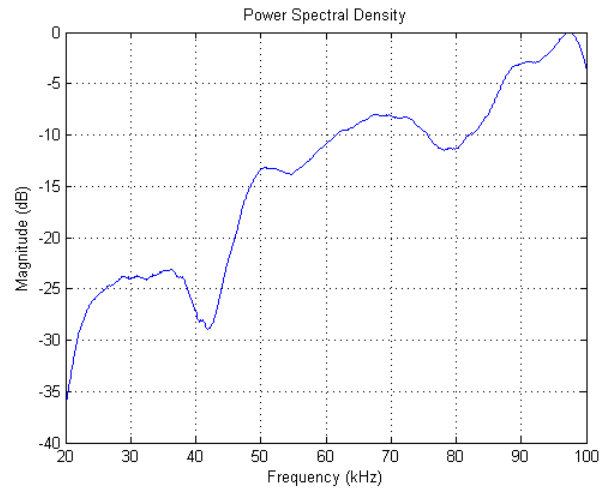


Figure 5. PSD of chirp signal at 1m (frequency response of emitter)

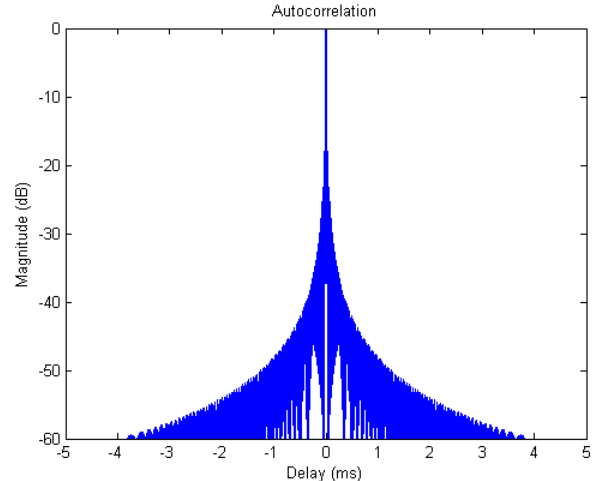


Figure 6. Envelope of original chirp waveform autocorrelation function

The custom transducer used in this experiment does not exhibit a flat response over the 20-100 kHz band. Figure 5 shows the PSD of the chirp signal that it emitted. The envelope of the autocorrelation function of the original chirp waveform with a flat response has a narrow main lobe and negligible sidelobes, as shown in Figure 6. The autocorrelation function of the chirp signal produced by the custom transducer is shown in Figure 7. The main lobe is wider, and the

sidelobes are stronger, averaging about -40 dB across the 10 ms spread. However, since the signal was received with high SNR ( $19 \text{ dB} < \text{SNR} < 58 \text{ dB}$ ), the distortion introduced by the sidelobes on the impulse response estimates was minimal.

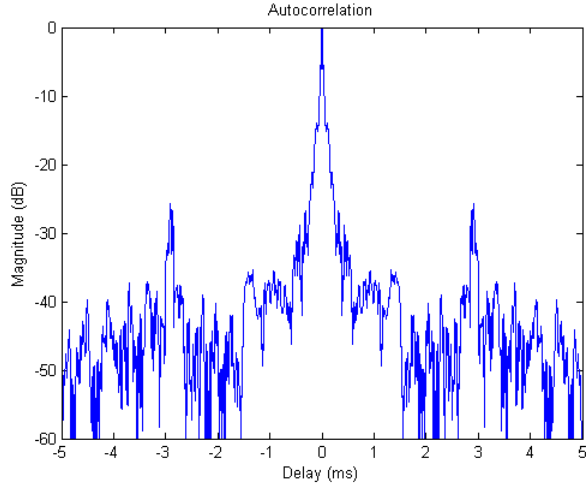


Figure 7. Envelope of emitted chirp waveform autocorrelation function

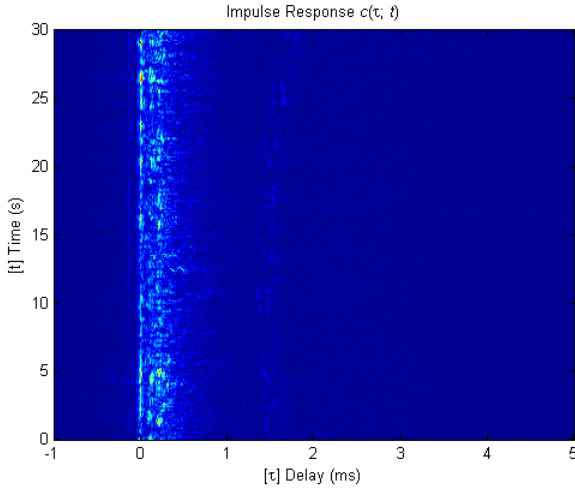


Figure 8. Successive time-variant impulse response estimates at 505m

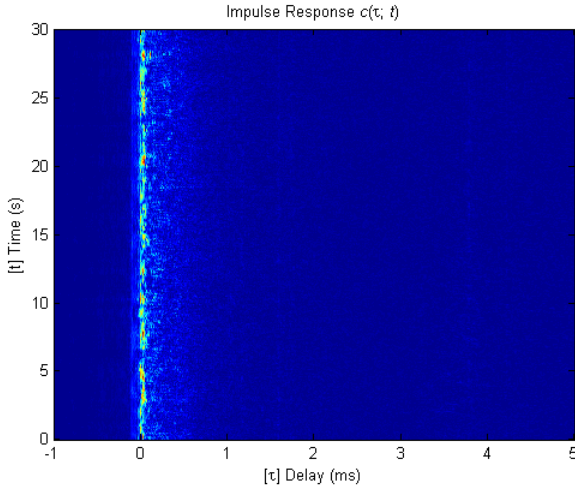


Figure 9. Successive time-variant impulse response estimates at 200m

Figure 8 shows 30 seconds of impulse response estimates  $c(\tau; t)$  of the Hudson River estuary at the 505-meter distance. While there is significant fluctuation in the amount of correlation, the strongest correlation always occurs within a 0.5-ms window. Three multipath components are present, though each has been subjected to periods of deep fading. Figure 9 shows the time evolution of impulse response estimates observed over the 200-meter channel. Deep fading is once again present, but it appears there is a single line-of-sight arrival over the shorter distance.

### B. Scattering Function

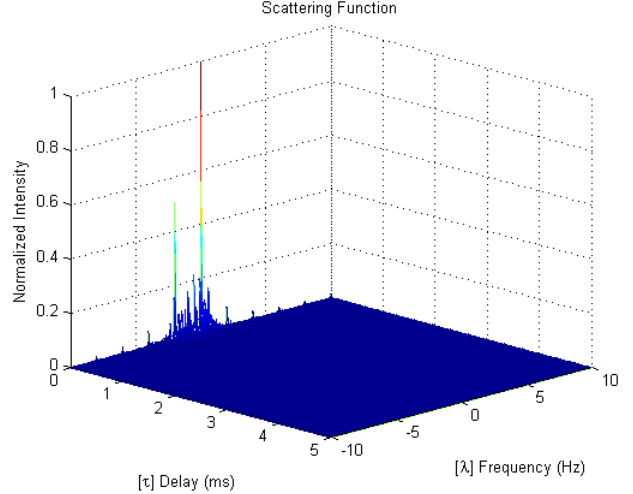


Figure 10. Scattering function at 505m

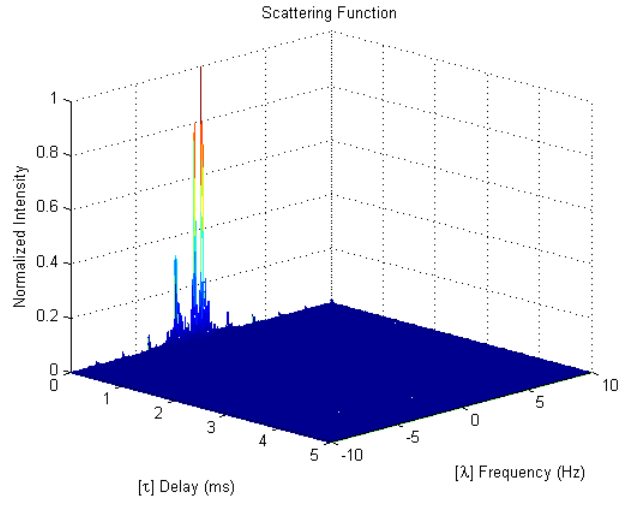


Figure 11. Scattering function at 200m

Assuming that  $c(\tau; t)$  is a WSS random process, the auto-correlation  $A$  of  $c(\tau; t)$  is defined as

$$A_c(\tau_1, \tau_2; \Delta t) = E[c^*(\tau_1; t)c(\tau_2; t + \Delta t)], \quad (2)$$

where  $*$  denotes the complex conjugate. Further assuming US – that the attenuation and phase shift of the channel at two

separate path delays  $\tau_1$  and  $\tau_2$  are uncorrelated,

$$E[c^*(\tau_1; t)c(\tau_2; t + \Delta t)] = A_c(\tau_1; \Delta t)\delta[\tau_1 - \tau_2] \triangleq A_c(\tau; \Delta t). \quad (3)$$

The scattering function is defined as the Fourier transform of  $A_c(\tau; \Delta t)$  with respect to the  $\Delta t$  parameter, as in

$$S_c(\tau; \lambda) = \int_{-\infty}^{\infty} A_c(\tau; \Delta t) e^{-j2\pi\lambda\Delta t} d\Delta t. \quad (4)$$

The scattering function gives the average power output of the channel as a function of time delay  $\tau$  and Doppler frequency  $\lambda$  and is the basis for computing the remainder of the channel characterization functions described in this paper. Figures 10 and 11 show the scattering function of the 505-meter and 200-meter channels, respectively.

### C. Multipath Intensity Profile

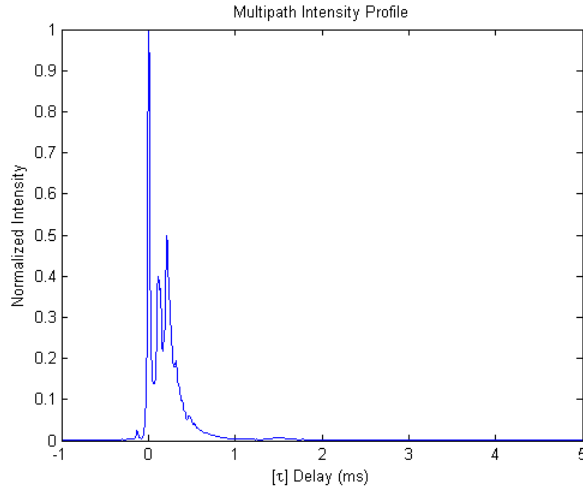


Figure 12. Multipath intensity profile at 505m

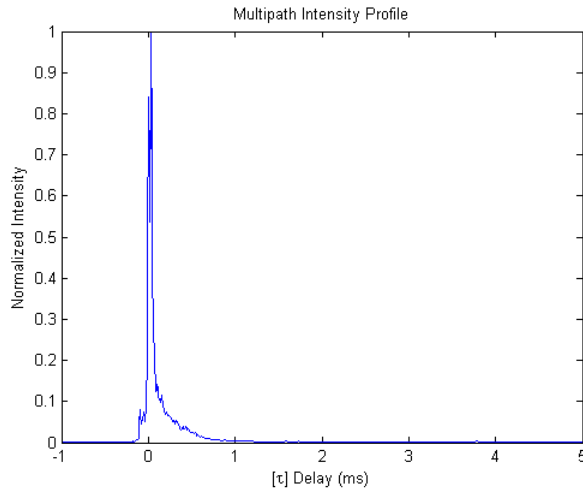


Figure 13. Multipath intensity profile at 200m

The multipath intensity profile (MIP) or power delay profile  $P(\tau)$  gives the average power output as a function of time de-

lay  $\tau$ . It is computed by summing the power levels over the  $\lambda$  values, as in

$$P(\tau) = \int S_c(\tau; \lambda) d\lambda. \quad (5)$$

Figure 12 shows the MIP derived from the scattering function of the 505-meter channel. There are three clearly defined multipath components occurring within a 0.5-ms window. Figure 13 shows the single-component MIP of the 200-meter channel. The Doppler shift and spread of the main multipath arrivals have been calculated using the method described in [5], which provides the average and rms delay spreads in Hz, as in

$$\text{shift}_{\text{Hz}} = \frac{\int \lambda |P(\lambda)| d\lambda}{\int |P(\lambda)| d\lambda} \quad (6)$$

$$\text{spread}_{\text{Hz}} = \sqrt{\frac{\int (\lambda - \text{shift})^2 |P(\lambda)| d\lambda}{\int |P(\lambda)| d\lambda}}, \quad (7)$$

where  $\lambda$  is the Doppler frequency in Hz and  $P(\lambda)$  is the power of the spectral component at frequency  $\lambda$ . Table I lists the Doppler shift and spread of the three strongest components of the 505-meter MIP and the single arrival found in the 200-meter MIP.

TABLE I  
DOPPLER SHIFT AND SPREAD (HZ) OF STRONG MULTIPATH ARRIVALS

	200m			505m		
	Time (ms)	Shift	Spread	Time (ms)	Shift	Spread
Arrival 1	0.010	-0.5029	2.0677	0.010	-0.7279	2.0831
Arrival 2	—	—	—	0.115	-0.6689	2.2931
Arrival 3	—	—	—	0.215	-0.7336	2.4141

By replacing  $\lambda$  with  $\tau$ , (6) and (7) can be reapplied to determine the mean excess delay and rms delay spreads of the MIP [14]. The threshold level was set to -20 dB, and the maximum excess delay was computed for multipath components within 10 dB of the maximum level. Table II lists the delay spreads obtained at the 200-meter and 505-meter distances.

TABLE II  
DELAY SPREAD OF MULTIPATH INTENSITY PROFILE (MS)

	Mean Excess Delay	RMS Delay Spread	Maximum Excess Delay
200m	0.1002	0.1490	0.1850
505m	0.1835	0.1625	0.4000

### D. Spaced-Frequency Correlation Function

The Fourier transform of the MIP yields the spaced-frequency correlation function (SFCF), which provides a measure of the frequency coherence of the channel. This function indicates the coherence bandwidth of the channel, which is a statistical measure of the range of frequencies over which the channel passes all spectral components with approximately equal gain and linear phase [15]. Figures 14 and 15

show the SFCF of the 505-meter and 200-meter channels, respectively, in dB scale. Table III lists the coherence bandwidth of the -3, -6, and -10 dB points.

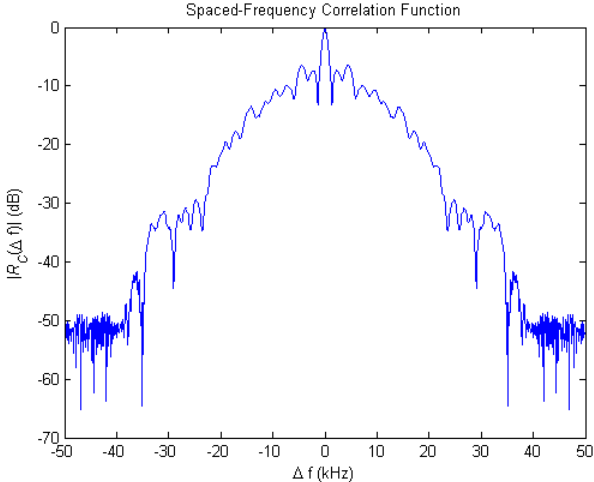


Figure 14. Spaced-frequency correlation function at 505m

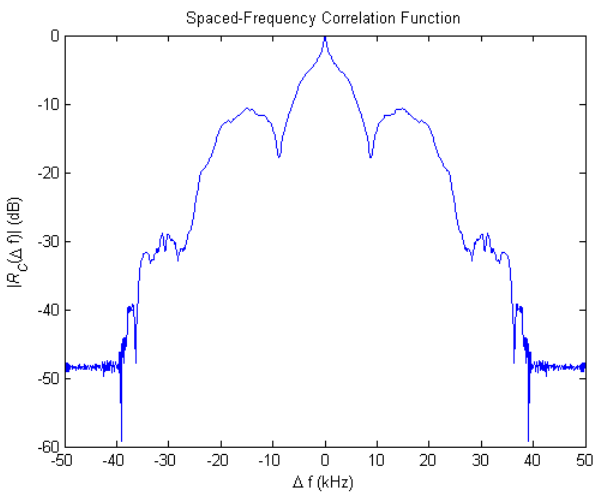


Figure 15. Spaced-frequency correlation function at 200m

TABLE III  
COHERENCE BANDWIDTH (Hz)

	-3 dB	-6 dB	-10 dB
200m	2165	7993	12323
505m	1166	1665	2165

#### E. Doppler Power Spectrum

The Doppler power spectrum provides the signal intensity as a function of the Doppler frequency  $\lambda$ . It is found by summing the power of spectral components over the time delay  $\tau$  of the scattering function, as seen in

$$P(\lambda) = \int S_c(\tau; \lambda) d\tau \quad (8)$$

The range of frequencies over which the Doppler power spectrum is essentially nonzero is known as the Doppler spread of the channel. Figures 16 and 17 show the Doppler power spec-

tra of the 505-meter and 200-meter channels, respectively. There is virtually no Doppler shift associated with the primary component in either of these spectra; however, other components do contribute to an overall shift and spread. Table IV lists this Doppler shift and spread, computed via (6) and (7).

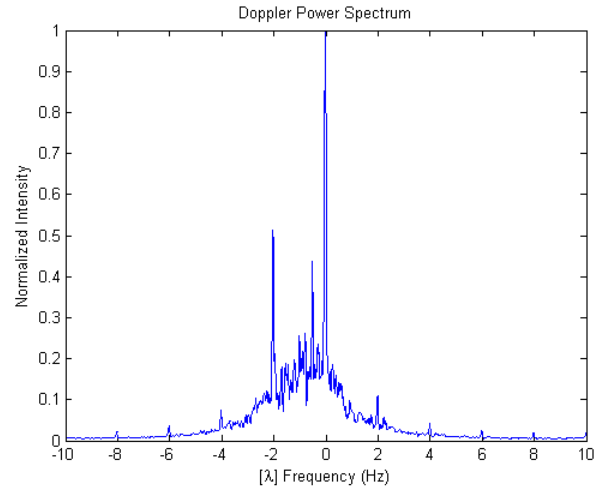


Figure 16. Doppler power spectrum at 505m

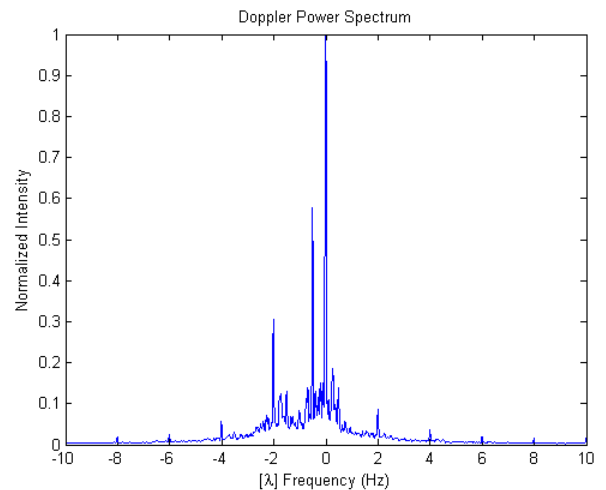


Figure 17. Doppler power spectrum at 200m

TABLE IV  
OVERALL DOPPLER SHIFT AND SPREAD (Hz)

	Shift	Spread
200m	-0.4806	2.9408
505m	-0.6237	2.8177

#### F. Spaced-Time Correlation Function

The Fourier transform of the Doppler power spectrum provides the spaced-time correlation function (STCF), which specifies the extent to which there is correlation between the channel's response to two sinusoids sent at different times. It provides the channel's coherence time, a measure of the expected time duration over which the channel's response is essentially invariant [15]. Figures 18 and 19 show the STCF of the 505-meter and 200-meter channels, respectively. Table

V lists the coherence times corresponding to correlations of 0.5, 0.25, and 0.1, which are equivalent to amplitude correlations of -3, -6, and -10 dB.

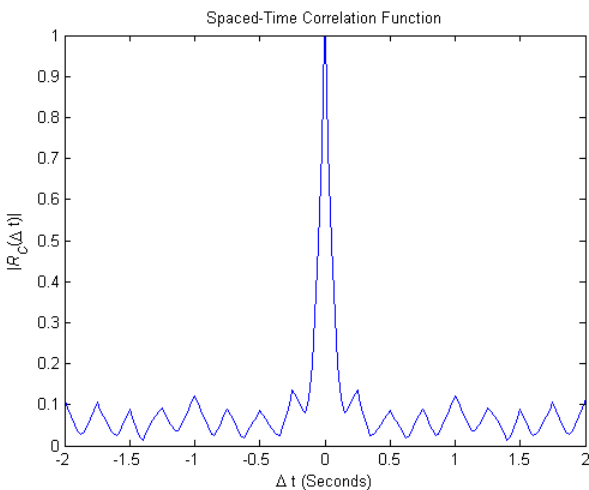


Figure 18. Spaced-time correlation function at 505m

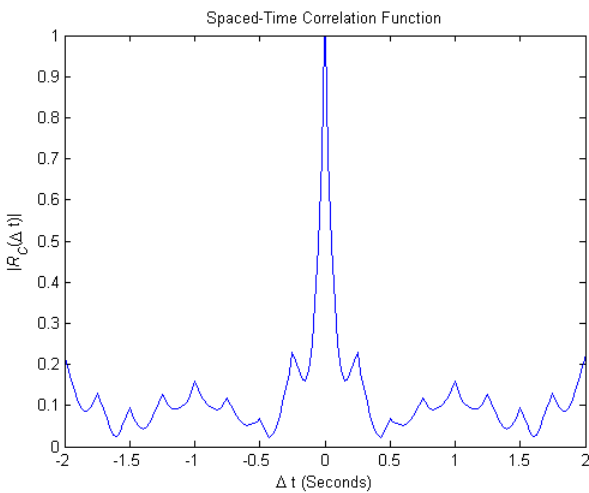


Figure 19. Spaced-time correlation function at 200m

- 3) The envelope of the signal was computed by taking its magnitude, as in

$$\text{envelope}_t = \sqrt{\text{real}_t^2 + \text{imag}_t^2}. \quad (9)$$

- 4) The fading envelope was normalized to zero mean.

Figures 20 and 21 show the channel-induced amplitude fluctuations of the 60 kHz sinusoid at 505 and 200 meters, respectively. The fluctuations in the received signal level are huge, varying more than 80 dB during the 1-minute test. Figures 22 and 23 show the cumulative distribution of amplitude levels of each of the 5 sinusoids. It appears that at both distances the channel affected all the sinusoids equally, with approximately a tenfold decrease in the probability for every 10 dB decrease in the signal level, at least for down to -50 dB relative to the mean level. It should be noted, though, the confidence intervals for points below -50 dB become significantly reduced, as there are relatively few low-amplitude samples in the 1-minute recording.

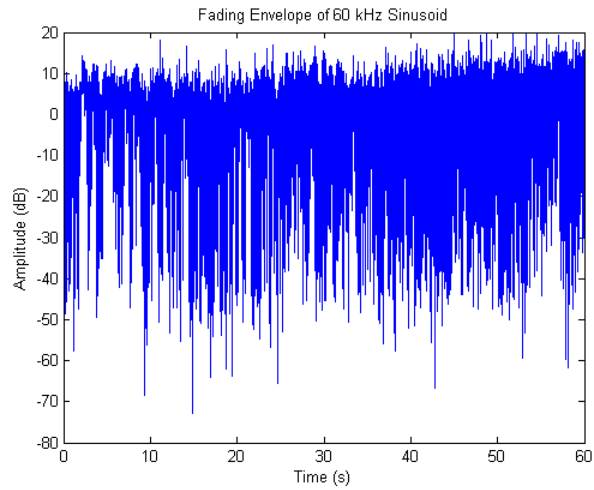


Figure 20. Fading envelope of 60kHz sinusoid at 505m

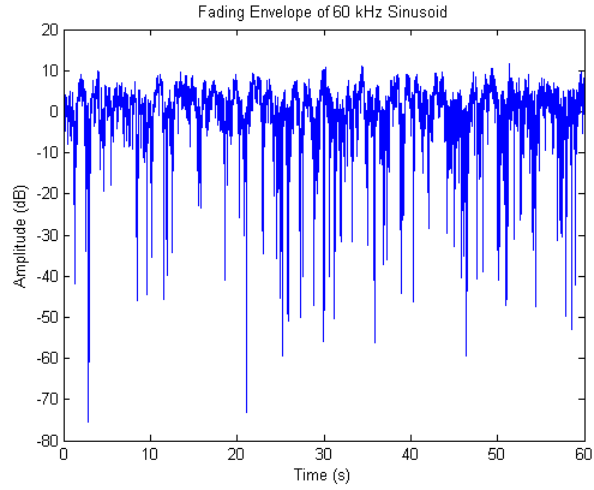


Figure 21. Fading envelope of 60kHz sinusoid at 200m

TABLE V  
COHERENCE TIME (MS)

	0.5 (-3dB)	0.25 (-6dB)	0.1 (-10 dB)
200m	50	150	650
505m	50	150	250

#### G. Fading Characteristics

The comb signal containing 5 sinusoids – 35, 45, 60, 75, and 85 kHz, where the frequencies were chosen so that no harmonics overlap – has been analyzed to determine the type of fading is present in the Hudson River estuary using the following procedure:

- 1) A 10<sup>th</sup> order band-pass Butterworth filter with a passband of 2 kHz was applied to each of the tones.
- 2) The analytic signal was obtained from the filtered data via the Hilbert transform.

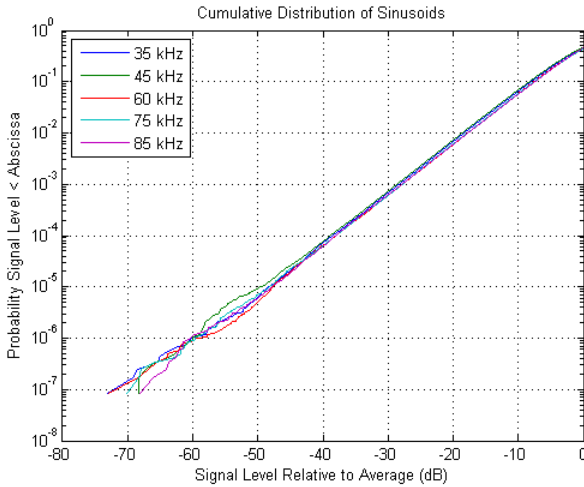


Figure 22. Cumulative distribution for fading measurements at 505m

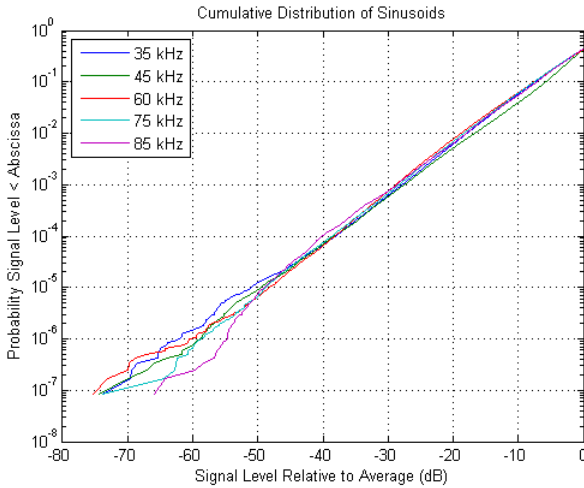


Figure 23. Cumulative distribution for fading measurements at 200m

Since 60 kHz is the mean frequency of both the chirp and comb signals, it was deemed the best candidate for use in determining the fading distribution. Maximum likelihood estimation was used to fit the data to the Rayleigh, Rice, and Nakagami- $m$  distributions, which are commonly used to describe fading channels, and to other less likely potential distributions, including gamma, beta, and lognormal.

The goodness of fit was tested with three different metrics. In all cases, the histogram of signal levels was divided into 100 bins.  $P$  is the probability distribution of the measurements;  $Q$  is the probability distribution of the fit. The first metric is Kullback-Leibler divergence [16],  $D_{KL}$ , defined as

$$D_{KL}(P \parallel Q) = \sum_i P(i) \log_2 \frac{P(i)}{Q(i)}. \quad (10)$$

The second metric is the Bhattacharyya distance [17],  $D_B$ , defined as

$$D_B(P, Q) = -\log_2(BC), \quad (11)$$

where  $BC$  is the Bhattacharyya coefficient,  $\sum_i \sqrt{P(i)Q(i)}$ . The third and final metric,  $D_{CRM}$ , is a metric based on the Bhattacharyya coefficient, proposed by Comaniciu, Ramesh, and Meer [18], defined as

$$D_{CRM}(P, Q) = \sqrt{1 - BC}. \quad (12)$$

Tables VI and VII provide the values of the three metrics as well as the log-likelihood ( $LL$ ) values obtained while fitting the distributions to the data. For each of the 3 metrics, lower values indicate less divergence from the actual data. In the tables, the best match for each metric is printed in bold.

TABLE VI  
GOODNESS OF FITS (505M)

	$D_{KL}$	$D_B$	$D_{CRM}$	$LL$
Beta	0.0439	0.0038	0.0514	3.14567e+007
Gamma	0.0471	0.0041	0.0533	3.14472e+007
Lognormal	0.3689	0.0212	0.1208	3.07398e+007
Nakagami- $m$	<b>0.0263</b>	<b>0.0037</b>	<b>0.0506</b>	3.13736e+007
Rayleigh	0.0413	0.0052	0.0600	3.13174e+007
Rice	0.0413	0.0052	0.0600	3.13174e+007

TABLE VII  
GOODNESS OF FITS (200M)

	$D_{KL}$	$D_B$	$D_{CRM}$	$LL$
Beta	0.0328	0.0083	0.0755	1.43424e+007
Gamma	0.0529	0.0136	0.0967	1.41509e+007
Lognormal	0.1803	0.0376	0.1604	1.30297e+007
Nakagami- $m$	0.0100	0.0026	0.0422	1.45294e+007
Rayleigh	0.0100	0.0026	0.0424	1.45291e+007
Rice	<b>0.0069</b>	<b>0.0016</b>	<b>0.0336</b>	1.45580e+007

In the 505-meter case, all three metrics revealed that the Nakagami- $m$ <sup>1</sup> distribution, where  $m = 0.889274$ , was the closest match. In the 200-meter case, when  $m = 1.00845$  in Nakagami, the Rician distribution was the best match in all three metrics. The results correspond with the depiction of the successive impulse response estimates in Figures 8 and 9. At 200 meters, it appears that there is a fairly strong line-of-sight component, which is what the Rician model describes. At 505 meters, the fading appears to be worse than Rayleigh, given

<sup>1</sup> The Nakagami- $m$  distribution can model a range of fading channels from one-sided Gaussian fading ( $m = 1/2$ , worst-case fading) to nonfading ( $m = \infty$ ).  $m = 1$  is a special case, equivalent to Rayleigh fading [19]. Some papers state that the Rician distribution can be closely approximated by the Nakagami- $m$  distribution when  $m > 1$ ; however, other references including [20] and [21] argue against that claim.

the low value for  $m$  in the Nakagami- $m$  distribution. Figures 24 and 25 show the histograms of the measurements and the curves corresponding to each of the 6 distributions for the 505-meter and 200-meter channels, respectively.

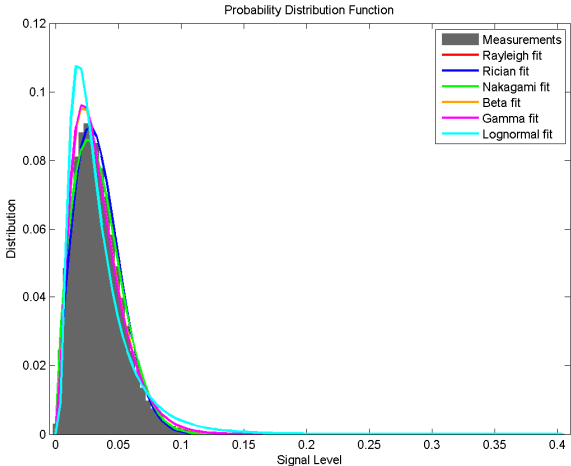


Figure 24. PDF of measurements and fits at 505m

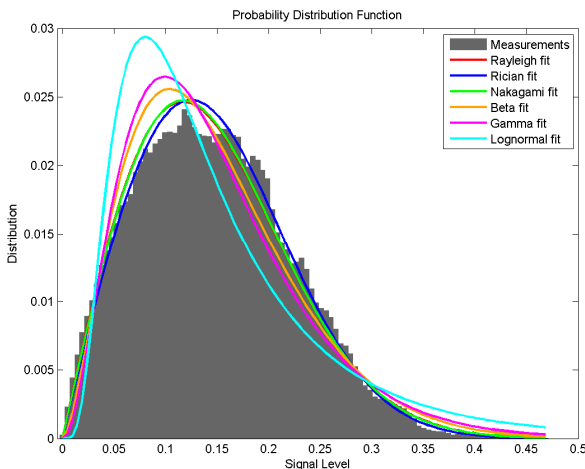


Figure 25. PDF of measurements and fits at 200m

#### IV. IMPLICATIONS FOR DIGITAL COMMUNICATION

Channel characterization is a pertinent step in designing a digital communication system for a particular environment. The values obtained in the analyses in Section III put a quantitative limit on some aspect of the system. The performance analysis alone is worthy of another paper; however, some general information will be discussed here.

The maximum excess delay of the channel  $T_m$ , derived from the multipath intensity profile, places a limit on the duration of a symbol,  $T_s$ . If  $T_m > T_s$ , the channel exhibits frequency-selective fading, which results in channel-induced ISI. In this case, the communication system will need to perform equalization to mitigate the distortion. If  $T_s > T_m$ , the channel exhibits flat fading, which does not result in ISI. For the 200-meter channel,  $T_m = 0.1850$  ms implies the system can transmit up to about 5400 symbols per second and still avoid ISI.

At 505 meters, that number drops to 2500 symbols per second. Some references advocate using the rms delay spread to estimate the symbol rate [15, 22], since different channels can exhibit different signal-intensity profiles over the delay span [15]. When using the rms delay spread values, the symbol rates rise to approximately 6700 and 6100 symbols per second for the 200-meter and 505-meter channel, respectively.

Time-spreading can also be viewed from the frequency domain. The SFCF yields the coherence bandwidth  $f$  of the channel. If  $W > f$ , where  $W$  is the bandwidth required for modulation, the channel imposes frequency-selective degradation. If  $f > W$ , the channel exhibits flat fading. No universal relationship exists between the coherence bandwidth and delay spread [15, 22], since the exact relationship is a function of specific channel impulse responses and applied signals [22]. It is also important to note that while the rms delay spread may yield some symbol rate, the actual bandwidth required by a certain type of modulation at that symbol rate may exceed the coherence bandwidth of the channel.

The STCF yields the time-variance of the channel in terms of the coherence time  $T_c$ . If  $T_s > T_c$ , fast fading degradation occurs, since the channel's conditions change within the duration of a single symbol. Such channels typically require non-coherent or differentially coherent modulation [15]. If  $T_c > T_s$ , the channel exhibits slow fading. The -3dB coherence time of the Hudson River estuary is 50 ms at both distances. As long as the symbol time is shorter than 50 ms, this channel is considered to be a slow fading channel.

The Doppler power spectrum provides a measure of the spectral broadening of the received signal caused by the rate of change in the channel. If the Doppler spread  $f_d > W$ , the channel is referred to as fast fading. If  $W > f_d$ , the channel is referred to as slow fading. If the baseband signal bandwidth is much greater than  $f_d$ , the effects of Doppler spread at the receiver are negligible [22].

Given all the values presented in this paper, the designer of the communication system can choose between a more robust modulation technique with a slower bit rate, for more accurate data transmissions and low processing overhead, and those offering faster transmissions at the expense of processing power and spatial techniques (arrays of hydrophones).

While some papers have characterized shallow water channels many kilometers in length, it is noteworthy that the Hudson River estuary degrades from Ricean fading at 200 meters to Nakagami- $m$  fading worse than Rayleigh at only 505 m. The fading most likely continues to become more severe at greater distances. If conditions are too harsh for small systems with limited processing power to mitigate, a multi-hop network of devices in close proximity can be deployed so that each acoustic link is more manageable.

#### V. SUMMARY

During a field test in August 2008, LFM chirp signals and a comb signal were emitted to characterize the Hudson River estuary. Environmental conditions were recorded. The chan-

nel's scattering function and derived functions have been presented. Values for Doppler shift and spread, delay spread, coherence bandwidth, and coherence time have been provided. Various distributions were fitted to amplitude fluctuations, and the channel was found to degrade from Ricean to Nakagami- $m$  fading worse than Rayleigh over increasing distances. Future experiments will characterize the channel at several other distances and emit different waveforms containing modulated data for offline analysis.

#### ACKNOWLEDGMENT

The author would like to thank Nikolay Sedunov and Alex Sedunov for their efforts in gathering data, Ionut Florescu for a discussion on distribution fitting, and Dan Duchamp for advice on writing this paper.

#### REFERENCES

- [1] M. Chitre, S. Shahabudeen, L. Freitag, and M. Stojanovic, "Recent Advances in Underwater Acoustic Communications & Networking," in Proc. MTS/IEEE OCEANS 2008. Quebec City, Canada, Sept. 2008.
- [2] J. Preisig, "Acoustic Propagation Consideration for Underwater Acoustic Communications Network Development," in Proc. WUWNet'06, Sept. 2006.
- [3] G. Loubet and G. Jourdain, "Characterization of the Underwater Medium as an Acoustical Horizontal Transmission Channel," in Proc. of the IEEE International Conference on Acoustics, Speech and Signal Processing, Vol. 1, pp. 329-332, April 1993.
- [4] G. Cook and A. Zakhnich, "Chirp Sounding the Shallow Water Acoustic Channel," in Proc. of the IEEE International Conference on Acoustics, Speech and Signal Processing, Vol. 4, pp. 2521-2524, May 1998.
- [5] S. Dessalermos, "Undersea Acoustic Propagation Channel Estimation," Master's Thesis, Naval Postgraduate School, Monterey, CA, 2005.
- [6] H. S. Dol, F. Gerdes, P. A. van Walree, W. Jans, and S. Künzel, "Acoustic channel characterization in the Baltic Sea and in the North Sea," in Proc. OCEANS 2008, Quebec City, Canada, Sept. 2008.
- [7] National Instruments USB-6221 DAQ Specifications. Accessed online: <http://sine.ni.com/nips/cds/view/p/lang/en/nid/203093>, Aug. 2009.
- [8] National Instruments PCI-6123 DAQ Specifications. Accessed online: <http://sine.ni.com/nips/cds/view/p/lang/en/nid/201938>, Aug. 2009.
- [9] International Transducer Corp ITC-6050C Preamplified Hydrophone Specifications. Accessed online: [http://www.itc-transducers.com/itc\\_page.asp?productID=29](http://www.itc-transducers.com/itc_page.asp?productID=29), Aug. 2009.
- [10] Urban Ocean Observatory at the Center for Maritime Systems, "NYHOPS Present Conditions Time Series and Downloads," Accessed online: <http://hudson.dl.stevens-tech.edu/maritimeforecast/PRESENT/data.shtml>, Aug. 2009.
- [11] Wave Information Studies (WIS) Direction Convention. Accessed online: <http://www.frf.usace.army.mil/wis/datadefs.html>, Aug. 2009.
- [12] R. J. Urick, *Principles of Underwater Sound*, Third Edition, Peninsula Publishing, 1996.
- [13] P. Bello, "Characterization of randomly time-invariant channels," IEEE Trans. Commun. Syst., Vol. CS-11, pp. 361-393, Dec. 1963.
- [14] A. Goldsmith, *Wireless Communications*, Cambridge University Press: Cambridge, 2005.
- [15] B. Sklar, *Digital Communications: Fundamentals and Applications*, Second Edition, Prentice Hall PTR: Upper Saddle River, 2001.
- [16] S. Kullback and R. A. Leibler, "On Information and Sufficiency," *The Annals of Mathematical Statistics*, Vol. 22, No. 1, pp. 79-86, 1951.
- [17] A. Bhattacharyya, "On a measure of divergence between two statistical populations defined by their probability distributions," *Bulletin of the Calcutta Mathematical Society*, Vol. 35, pp. 99-109, 1943.
- [18] D. Comaniciu, V. Ramesh, and P. Meer, "Kernel-Based Object Tracking," IEEE Transactions on Pattern Analysis and Machine Intelligence, Vol. 25, No. 5, pp. 564-577, May 2003.
- [19] M. Nakagami, "The  $m$ -Distribution – A General Formula of Intensity Distribution of Rapid Fading," in W. C. Hoffman (ed.): *Statistical Methods in Radio Wave Propagation*, Pergamon Press: New York, 1960, pp. 3-36.
- [20] Jean-Paul M.G. Linnartz (ed.), "Comparing Rician and Nakagami Fading," *Wireless Communication Reference Website*, Accessed online: <http://www.wirelesscommunication.nl/reference/chaptr03/ricenaka/ricenaka.htm>, Aug. 2009.
- [21] M. D. Yacoub, G. Fraidenraich, and J.C.S. Santos Filho, "Nakagami- $m$  phase-envelope joint distribution," Electronics Letters, Vol. 41, Issue 5, pp. 259-261, Mar. 2005.
- [22] T. S. Rappaport, *Wireless Communications: Principles and Practice*, Second Edition, Prentice Hall PTR: Upper Saddle River, 2002.